# Dry Electrodes with a Printed Cellulose-Graphene Ink for Low-Profile Strain Sensors in Electromyography

*Allyson R. Tesky[1], McKenna Hicks[2], Sujan Aryal[3], Brendan Jones[3], Julia Molitor[4], and Anupama B. Kaul[3,5*]*

[1]Department of Biomedical Engineering, [2]Department of Computer Science and Engineering [3]Department of Electrical Engineering, [4]Department of Mechanical Engineering, [5]Department of Materials Science and Engineering, University of North Texas, Denton, TX 76203, U.S.A.

*Corresponding Author Email: anupama.kaul@unt.edu

## ABSTRACT

Dihydrolevoglucosenone, commonly known as Cyrene, is a renewable and fully biodegradable cellulose-waste derived, environmentally friendly solvent, presenting a non-toxic alternative to N-methyl-2-pyrrolidone (NMP). Currently, solution-based processing of graphene and other similar van der Waals solids favor toxic solvents such as NMP, limiting their use for biosensing. However, with the use of Cyrene, bio-compatible printable devices are possible, and studies have already demonstrated its use in temperature and other biosensing methods through screen-printing. Screen-printing unfortunately often requires masks that constrain the minimum acquirable feature size to be above hundreds of centimeters and wastes material, adding to process complexity and cost. Conversely, inkjet-printing is an attractive alternative for the maskless patterning of hierarchically assembled structures, with micron length scales attainable. Graphene's high conductivity positions it ideally for long-wear sensors such as dry electrodes or respiration monitors. Here, we demonstrate the potential of Cyrene-based graphene inks through few-layer inkjet printing on flexible substrates for the first time, to produce non-toxic conductors toward a strain-mediated mechanism for biosensing, used to detect bodily motion for wearable electronics. The challenges overcome in this study include engineering ink chemistry and printing parameters such that Cyrene's relatively high viscosity compared to typical inkjet solvents, still allows for droplet ejection in a conventional material printer, yielding well-resolved clean line-edges in contrast to other solvents that exhibit diffuse line-edges possibly from stray droplets and ink-splashing. Temperature-dependent transport measurements on the inkjet-printed Cyrene-based graphene films showed the conductivity to be largely temperature-invariant but at lower temperatures below 100 K, conductivity decreased, likely as a result of increased inter-membrane separation arising from thermal contraction. Additionally, temperature-dependent Raman spectroscopy showed the red-shift in the G-band, 2D-band and D-band peaks, as temperature increased. By validating flexion motion detection of the proximal interphalangeal joint demonstrated in this study, our work is the first of its kind to successfully additively manufacture inkjet-printed Cyrene-based graphene strain sensors on flexible substrates for bio-sensing and wearables.

**Keywords**: graphene, biocompatible inks, sustainability, wearable electronics, biosensors, strain sensors, flexible electronics, printed electronics

## 1. Introduction

As the medical industry progresses to include more at-home care options, the need for non-invasive, low-profile, and re-usable biosensor options expands in parallel. Notable biosensors include strain sensors and electrodes. Strain sensors are often used in respiration monitors and also have potential in soft robotics and prostheses[1-4]. Other sensing modalities include electromyography (muscle signals), electrocardiography (heart signals), and electroencephalography (brain signals)[5-7], where electrodes are used to capture the action potentials generated by the body during signaling. The current established standard for surface electrodes utilizes a silver/silver chloride (Ag/AgCl) sensing element with conductive gel technology as its basis. However, the acclimatization time to adjust to the skin after placement is one of the primary disadvantages for these wet-electrodes, even though it yields the lowest skin-interface impedance of any surface electrode due to the characteristic electrolytic gel that forms a seal against the skin. Other downsides of these electrodes include the irritating adhesive, requirement of skin abrasion, single usability, attenuation of the signals after long periods of operation, and a raised profile that obstructs usage since the electrodes catch and rub against clothing, motivating the need for reusable and low-profile sensors for biosensing[7-12].

While the function of the electrodes remains the same across signal and electrode types, the configuration of the electrodes and accompanying circuit will vary. Electromyogram (EMG) signals are one of the simplest to capture as they only require a pair of bipolar electrodes connected to a differential amplifier circuit to measure the voltage between each point of contact. Moreover, EMG signals are easy to capture and recognize with limited equipment compared to electrocardiograms (ECG) or electroencephalograms (EEG); the latter techniques require more care towards electrode placement and more sensitive circuits with higher noise rejection. Thus,

this positions EMG ideally as a platform for the prototypical demonstration of experimental electrodes in the exploration of human-machine interfaces for prosthetic control[6,9]. While EMG principles are at the heart of detecting muscle activation and intensity, prosthetic systems relying on broader sensing and detection mechanisms, including strain-based sensors, may offer unique capabilities and solutions than those enabled by EMG principles alone. When considering locomotion of the body and designing soft robotics, it is important to consider the deformation of these structures, whether it is a stimulus used to direct the mechanics, or control against environmental stimuli[3,13]. As such, low-profile, flexible strain sensors may assist in fine-tuning movements or developing feedback systems in prosthetic structures.

Graphene represents a suitable material for both strain sensors and low-profile dry electrodes. As a single sheet of carbon atoms arranged in a two-dimensional (2-D) honeycomb lattice, graphene has a high carrier mobility, strength, flexibility, biocompatibility, and versatility, making it an ideal material for nanoelectronics and more recently for biosensing[8,11,14-18]. Furthermore, a wide variety of synthesis and manufacturing methods exist for the realization of graphene which include, micro-mechanical exfoliation, chemical vapor deposition (CVD), and liquid-phase exfoliation (LPE)[14-16,19, 20]. Of these methods, LPE is of keen interest, especially for translational research, due to its potential scalability in industrial settings[16,19-21]. Liquid-phase exfoliation is a method in which graphene is produced from dispersing graphite powder in a solvent and applying energy through ultrasonication or high-shear mixing to disrupt the inter-layer van der Waals bonds and produce a suspension of single-layer or few-layer membranes, known collectively as the ink[14, 16,19]. These inks may be produced with a variety of solvents, both aqueous and non-aqueous, but are most commonly made with N-methyl-2-pyrrolidone (NMP), dimethylformamide (DMF), and

a combination of cyclohexanone and terpineol (C/T), with or without the binder ethyl cellulose (EC)[12,14-24].

Deposition methods for graphene inks vary as much as the manufacturing methods, including spray-coating[4,16], screen-printing[15,19,20], and inkjet-printing[15,25]. Of these, the most common method is screen-printing due to its ease and ability to produce thick films in a single pass[20]. However, inkjet-printing is a promising technique for high accuracy placement and is more suitable for rapid prototyping compared to either spray-coating or screen-printing, as it can produce complex, hierarchically-assembled structures without the need for masks or screens[14,26], though the former has a higher upfront cost than other LPE approaches[16,19]. While graphene has shown promise towards wearable electronics and biomedical devices, traditional solvents used for graphene inks are known to be toxic, motivating a need for alternative solvents.

One of the most popular methods to circumvent the use of toxic solvents includes the suspension of hydrophilic graphene oxide (GO) flakes in non-toxic solvents that graphite is otherwise incompatible with, including water[27,28] and alcohol[28,29], amongst others[30,31]. After deposition, this suspension can be reduced via sonication or through thermal means[31], as well as electrochemical methods[29], yielding reduced graphene oxide (rGO). The properties can be enhanced further for bringing rGO closer to that of pristine graphene through the removal of oxygen-containing groups[29-31]. However residual defects and functional groups in the rGO remain even after reduction, comprising its full potential[30], and thus the motivation to examine alternative solvents is still an active area of research.

Dihydrolevoglucosenone, commonly called Cyrene, is one such emergent alternative to DMF and NMP[16,19,22,32,33]. As a biomass-derived, cellulose-based solvent produced by Circa since 2014[21], Cyrene is not only bio-degradable and renewable, but also non-toxic and capable of

delivering higher concentrations of graphene within the ink dispersion compared to the similarly behaving dipolar aprotic solvent, NMP[19, 22,32]. Cyrene-based graphene ink has been demonstrated in both spray-coating[16] and screen-printing[19,20], and while it has recently been used as an additive (4.3 wt.%) for improving poly(3,4-ethylenedioxythiophene) and polystyrene sulphonate-based ink in inkjet printing[34], it has yet to be demonstrated as the primary solvent for inkjet-printed graphene. One of the reasons for this is its high viscosity[22], which makes it more difficult to print reliably, but this challenge can be overcome by engineering the printing parameters and printer settings, as we demonstrate here.

In this paper we have successfully used Cyrene-based graphene inks for inkjet-printed wearable biosensors with a focus on conductors which facilitate the development of experimental electrodes as well as on strain sensors, potentially useful in soft prostheses and respiration monitors[3,4]. To establish a baseline for production of alternative biosensors, commercial electrodes were evaluated with a breadboard-built electromyogram for signal-to-noise ratio (SNR) determination—the details of which are available within the Supplementary Information (SI) section. Prior to printing, characterization of our Cyrene ink and the ensuing films was conducted using Raman spectroscopy and temperature-dependent dc electronic transport measurements. This ink was then used to realize graphene-based strain sensors, which has been previously demonstrated on a variety of substrates including film, fiber, foam, and hydrogels[4], but not generally through inkjet printing. In the case of fiber-based strain sensors, conductive networks can either be created with wet-spinning or surface modification. These fiber-based graphene sensors can be worn directly on the body and even integrated into clothing, with some washability to allow for a breathable and reusable biosensor[4,35]. However, biosensing with graphene is not limited to strain sensors alone, and it may also be used for electrochemical sensing of biomarkers such as glucose, folic acid,

dopamine, or even cancer-related proteins[36]. Other external sensors are also possible such as graphene-based electrodes, which can benefit similarly from flexible and reusable substrates. This work explores the additive manufacturing and inkjet printing of graphene with Cyrene on flexible polyimide (PI) substrates, where we have successfully demonstrated strain-dependent sensing with dry electrodes, overcoming some of the limitations of wet, gel-based electrodes commonly used in EMG[37]. This was done through flexion motion detection of the proximal interphalangeal joint, where our work is the first of its kind to successfully additively manufacture inkjet-printed Cyrene-based graphene strain sensors on flexible substrates for bio-sensing and wearables. The environmentally friendly and non-toxic nature of this solvent has promise not only for wearables, but also in agricultural and food industries, where sensors need to be safe for potential contacts made to food supplies.

## 2. Results and Discussion

### 2.1 Cyrene-based graphene ink synthesis and characterization

While commercial electrodes for EMG have enabled significant insights into muscle activity towards prosthesis, prosthetics, and wearable electronics applications, there is a well-accepted notion for the advantages of dry electrode technologies, including in flexible formats[38], to detect muscle and joint motion. Dry electrodes for surface EMG (or sEMG) excel where there are large muscle groups near the surface of the skin[5,7], but this practicality becomes more limited at locations where several muscle groups must interact to create motion or in complex joints, such as the shoulder[39] or the knee involving rotational movement[40], or in areas of the body comprised of low muscle mass, such as the hand. The demand for flexible and dry electrode arrays may prove particularly valuable to allow for the study and translation of complex joints for usable signals in

prosthetic control, including as supplements to existing systems[41,42]. Motivated by this need, we proceeded with our exploration of 2D materials, specifically graphene, to use new solvents for its LPE toward the formation of a viable ink for printing sensing devices to detect bodily motion at joints. For formulating the graphene ink, adequate characterization and understanding of the ink properties is necessary, especially as compared to a traditional solvent such as C/T with binder EC.

Though there are binder-free methods of formulating graphene inks[15], research with Cyrene is still in its infancy and has yet to demonstrate evidence towards one method or the other. Regardless, as binders can assist in maintaining graphene flake separation[19] and have been reported in improving substrate adhesion[15], a compatible binder, cellulose acetate butyrate (CAB), was added to the Cyrene prior to ink formulation, detailed in Section 2.2. To characterize the long-range order and quality of resultant flakes, Raman spectroscopy of our graphene films was used here, similar to previous well-established studies[8,14,16,19-21,43-46]. Raman spectroscopy data, conducted with a 532 nm excitation laser, are shown in **Figure 1(a)** for the Cyrene-based graphene ink, and the results are compared to the spectra obtained using the conventional solvent C/T in a ratio of 70:30 cyclohexanone:terpineol, 25 mg/ml graphite powder, and 20 mg/ml EC, with a laser wavelength of 633 nm. The inset in **Figure 1(a)** depicts the graphene-Cyrene ink to be dark and optically absorbing. Provided there is no interfering photoluminescence, the Raman spectra for graphene with varying excitation lasers used in the visible region should yield largely similar results[47]; though absolute intensities may vary with the lasers used, intensity ratios should reveal attributes of the actual material properties, independent of the laser. In this regard, the lower D/G intensity peak ratio, ~ 0.34 for the Cyrene-graphene film, compared to that of the C/T synthesized graphene film where the ratio was calculated to be ~ 0.40, indicates fewer defects in the former,

as observed in prior studies as well[19,43,46]. Additionally, the 2D/G-peak intensity ratio for the Cyrene ink was higher, ~ 0.422 compared to the C/T ink, where it was ~ 0.362. This is suggestive of Cyrene's greater effectiveness in exfoliating thinner membranes, although a ratio of two or three is representative of single-layer membranes and higher ratios may also be suggestive of doping[43]. **Table 1** summarizes the parameters obtained using Raman analysis for both inks. Overall, our results corroborate the findings of a previous study[19] that used a similar ink composition, both with and without CAB, which showed lower defects and no significant structural changes from the use of the binder.

Further characterization was performed on the Cyrene-based graphene through temperature-dependent Raman spectroscopy conducted from 77 to 800 K in atmospheric air, to decipher how the phonon spectra are modulated and possible interactions of phonons with defects, while at the same time shedding insights into their mechanical and thermal robustness in extreme environments. Being able to survive extremes in temperature may indicate potential use of our sensor in unusual thermal environments, such as deep space, hot planetary bodies, diving suits, and off-world machinery. To perform the temperature-dependent Raman measurements, the graphene ink was spin-coated onto an $SiO_2$ /Si substrate, where cooling was performed with liquid Nitrogen (LN2) down to 77 K, and the vibrational spectra were gathered in 50 K increments with heating through a heating stage up to 800 K. Four locations on the sample were selected for this measurement. Raman measurements were taken in each location by moving the laser spot to separate locations, before altering the temperature for the next set of temperature-dependent measurements. The sample was allowed to reach steady-state and equilibrate at its new temperature, prior to acquiring the data and this methodology was used from 77 K to 800 K in the rising cycle, and again from 800 K to 77 K in the temperature descending cycle. The data were

averaged for the peak locations over the four sites during the upward-cycle and similarly for the downward-cycle. The difference in the Raman shift and the full-width at half-maximum (FWHM) of the peaks between the cooling or heating cycle appeared insignificant, indicating little hysteresis in the data—please see the SI section (Figures S2 and S3) for further details. **Figure 1(b)** displays the representative temperature-dependent Raman spectra, where both the intensity and the Raman shift are shown simultaneously. The evident red-shift in all the graphitic peaks as the temperature increased is seen here but visualized in more detail in **Figures 1(c)-(e)**. Moreover, one of the characteristic CAB peaks[48] was also visible in the spectra of the graphene ink in the prior mentioned Cyrene/CAB study[19] which appeared at 2937 $cm^{-1}$. While this peak can still be observed in the temperature-dependent Raman characterization of our graphene films, the intensity of this peak at 2937 $cm^{-1}$ is far lower than those attributed to the dominant graphitic G-, 2D- and D-peaks, as seen in **Figure 1(b).** Additionally, when Raman characterization was conducted on the CAB film alone, as detailed in **Figure S5** of the SI section, no discernable peak-shifting is observed, despite its far reduced intensity, nor is there a marked change in intensity values as a function of temperature; this is unlike the observations made on the graphitic peaks. These point to the possible degradation and decomposition of the CAB during the film annealing process, as intended.

Though there appeared to be some nonlinear effects seen in the D- and 2D-peak locations with temperature, the trend nonetheless was similar for the red-shift observed. Although this is expected[49-52], as red-shifting is generally associated with material expansion upon heating, the FWHM, pictured in **Figure 1(f)**, was largely temperature invariant save for the 2D-peak, affirming the results observed in other studies[49] which have seen a gradual increase in the FWHM of the 2D-peak above 300 K. The invariance we find here may be uniquely attributed to the use of Cyrene

as the dispersing media, though more detailed experiments are necessary to more concretely validate this. With no noticeable difference in peak shape observed over the wide range of temperatures examined, from 77 K to 800 K, there appears to be little indication that mechanical robustness and thermal behavior through adhesion to the substrate is hindered in any noticeable way. This further suggests the promise of such emergent materials as the sensing media in extreme thermal environments.

Prior to proceeding with inkjet printing, further characterization of the ink was necessary to ensure it was appropriate and lent itself to printing due to concerns about its high surface tension and viscosity[22]. Invoking the Reynolds (*Re*) and Weber (*We*) numbers, which are used to theorize the behavior of a fluid while printing, a parameter *Z* is introduced that is inversely related to the Ohnesorge (*Oh*) number[53-57]. Together, these fluidic parameters are used to evaluate jettability according to,

$$Oh = \frac{1}{Z} = \frac{\sqrt{We}}{Re} = \frac{\eta}{\sqrt{\gamma \rho a}} \quad (1)$$

where $Re = v\rho a/\eta$ and $We = v^2 \rho a/\gamma$. Here, $v$ is the drop velocity, $\rho$ is the fluid density, $\gamma$ is the surface tension, $\eta$ is the dynamic viscosity, and $a$ is the nozzle width. For adequate printing a range of $1 < Z < 10$, corresponding to $0.1 < Oh < 1$, is generally appropriate[54-56]. The relationship between *Oh* and *Re* can be used to visualize the "printable fluid" window, which can be seen in **Figure 2(a)**. Values outside of this window may still be printable, but often result in non-optimal printing which includes splashing and satellite droplets. While it may be noted that C/T and Cyrene as pure solvents are both within the printable range, graphene and additives such as binders can further affect the resulting viscosity.

Low concentrations of binders are adequate to ensure ink stability, and concentrations higher than 1 mg/mL (CAB-to-Cyrene) can negatively affect dynamic or sheet resistance[19]. For these reasons, CAB was added in increasing amounts, starting at low weight percentages and the resultant viscosity was then measured at ambient temperature (20°C). Measurements for $\eta$, as in **Figure 2(b)**, were taken using a rheometer equipped with a small sample adapter, starting with pure Cyrene and progressively increasing the CAB content. In all recorded viscosity measurements, it took several seconds for the rheometer measurement to stabilize, evident from the inset data in **Figure 2(b)**, particularly for the more viscous formulations. As expected, however, higher concentrations of the binder also resulted in higher steady-state viscosity.

Because a low concentration of CAB is desirable for ensuring higher conductivity, the optimized wt.% for CAB in Cyrene was below the 0.08 wt.% mark, or roughly 1 mg/mL CAB for a volume of 10 mL Cyrene[21]. The resulting Cyrene mixture had $\eta$ ~ 13-14 cP which is a higher $\eta$ compared to commonly used inkjet solvents such as NMP, where $\eta$ ~ 1.7 cP[14], but it is still within the target range of 8-15 cP for good printing characteristics[24]. Furthermore, inks between 2 to 50 cP are also eligible for printing but may require additional accommodations for even jetting[53]. Once it was verified that Cyrene may be suitable for printing with the addition of CAB, an ink was developed via horn-tip sonication, the progress of which can be seen in **Figure 2(c)**. Here we clearly observe the final ink to be homogeneously black from the presence of graphene flakes and evenly dispersed without signs of sedimentation in the right-most vial. On the other hand, pure Cyrene is transparent (left-most vial) and the addition of CAB renders the solution darker in tint (middle-vial). Adding graphite powder to the ink slightly increases $\eta$ but this change is largely negligible. More notable is the change in surface tension from the addition of the graphite powder and binder. This can be estimated easily via the capillary rise method, using the following,

$$h = \frac{2\gamma \cos(\theta)}{\rho g r_0} \quad (2)$$

where the contact angle θ is measured via a drop shape analyzer using the Dataphysics measurement system (specifically, the optical contact angle goniometer and drop shape analysis system), $h$ is the rise of the fluid in the capillary, g is the acceleration due to gravity, and $r_0$ is the radius of the capillary. While we may use the $\gamma$ of the inks to estimate their *Z*, the addition of suspended particles in the solvents is expected to decrease this value[58], making it worthwhile to calculate $\gamma$ directly. Using the measured $\rho$ at ~1.28 g/ml and ~1.0 g/ml for the Cyrene and C/T inks, respectively, and with an $r_0$ ~ 0.42 mm, $h$ ~ 12 mm for the Cyrene ink and ~ 9 mm for the C/T ink, and $\theta$ ~ 48° for the Cyrene ink and $\theta$ ~ 26° for the C/T ink, $\gamma$ is the only unknown remaining. With this method, $\gamma$ for the Cyrene ink is estimated to be ~ 47.8 dynes/cm, below that of 72.5 dynes/cm for pure Cyrene[55], while for the C/T ink $\gamma$ ~ 20.9 dynes/cm, below the 33 dynes/cm expected for the of C/T[54].

Jetting of the produced ink may be viewed in **Figure 2(d)**, where **(i)** shows a cross-sectional view of the nozzles prior to drop formation, and **(ii)-(iv)** illustrate the progression of these drops as they exit the nozzle towards the drop watcher pad. While these droplets have moderate uniformity among them, it can be noted that they are at a relatively higher *v* due to the length of their "tails".[40] Shorter tails with more noticeable droplet heads are preferred, but through our experiments this was not possible at all due to the need for higher jetting voltages given the high $\gamma$ (72.5 dynes/cm[45]) of the Cyrene, and therefore a lower *We*. Though lower jetting voltages may be preferred, these however, did not produce droplets since there was insufficient energy for drop formation[41–40].

High $\gamma$ associated with low *We* make it difficult for the piezo-actuated nozzles to displace the air required for priming the jetting mechanism. To fulfill these priming requirements, typical values of $\gamma$ range from 20 to 40 dynes/cm[53], but $\gamma$ outside of window can be accounted for by changing $\rho$ or $v$ of the ink during formulation or through printer settings, respectively. The impact of $\eta$ and γ on printed lines can be noted in **Figure 2(e)** between printed C/T-based ink at **(i)** low, and **(ii)** high-magnifications, respectively, and similarly for printed Cyrene-based ink at **(iii)** low, and **(iii)** high-magnifications, respectively. The C/T ink has a lower $\eta$ and γ, and there is evidence for splashing in **(i),** in contrast to Cyrene with a far cleaner edge profile where minimal stray droplets or splashing is evident in **(iii)**. To determine if these defects are attributable to the *Z*-value discussed in Equation (1), it is worthwhile to estimate these values for the C/T and Cyrene-based inks.

Although the γ of our ink is unknown, using the γ values available for these solvents allows for a reasonable estimation of the *Oh* number, and therefore *Z*. The measured $\eta$ for the solvent/binder concentrations used for these inks were 5.85 cP and 13.78 cP for C/T + EC and Cyrene + CAB, respectively. Including the approximate γ of 20.9 dynes/cm and 47.8 dynes/cm with the associated $\rho$ of the solution and the nozzle width of 20 μm, the *Z* values are estimated to be ~ 3.50 and 2.54, respectively. Interestingly, a splattering effect is visible on the edge of the C/T-based ink in **(ii)** due to the presence of satellite droplets despite $1 < Z = 4.27 < 10$, compared to the Cyrene-based ink which is jetted relatively evenly on the $SiO_2$/Si substrate, and also contains a *Z*-value within the optimal range.

The C/T-based ink may have a high enough *Re* that despite an adequate *Z*-value, it has reached the "splashing region"[54,56]. Adding a higher concentration of EC to the C/T ink to increase its viscosity could improve these results by reducing the *Re*. Certainly, Cyrene has a distinct

advantage in this regard, as the amount of binder necessary is much lower compared to C/T, where the latter may require as much as 3 wt.% EC to reach the recommended viscosity; this is exacerbated in the case of DMF and NMP, which may need up to 4 and 6 wt.% EC, respectively, to reach this same range[54]. A scanning electron microscope (SEM) image of the Cyrene-based graphene film on $SiO_2$/Si, comprising of just three printed passes, is seen in **Figure 2(f)**, which further reveals its dense morphology, despite the relatively few passes used. In the case of C/T and other conventional solvents, typically 20 – 50 passes are needed, which not only increases device fabrication time, but also cost and printer instrumentation wear, challenges that are overcome here through our Cyrene-based ink and its unique attributes.

In addition to the Cyrene-based sample printed on $SiO_2$/Si, another sample was printed on polyimide (PI) substrates using the same conditions. Polyimide is of interest due to both its flexibility, and thus potential for strain sensing, as well as its biocompatibility that may allow it to be used in bio-electrode fabrication[8,11,17,18]. Both samples were evaluated using a Lakeshore Cryogenic probe stage for temperature-dependent dc transport measurements, as seen by the current-voltage (*I-V*) characteristics captured in **Figure 3(a).** The data in **Figure 3(a)-(i)** provides the *I-V* sweeps from -20 V to +20 V over a temperature range of 4 K to 350 K, with compliance set at ~ 1 mA. Closer inspection into the differences in current from 18-20 V in **Figure 3(a)-(ii)**, shows current saturation for graphene on the $SiO_2$/Si substrate at 350 K, but the film printed on PI had lower conductivity and did not reach current saturation at any temperature in the range tested. Here we tabulate the dynamic resistance, $R_{Dynamic}$, as the ratio of the instantaneous *V to I,* defined as $R_{Dynamic} = dV/dI$. The calculated $R_{Dynamic}$ is illustrated in **Figure 3(b)**. It was notable that at very low temperatures (~ 4 K), the $R_{Dynamic}$ was much higher in both samples, but it stabilized at around 100 K on the $SiO_2$/Si substrate, while this stabilization temperature was much lower, ~

10 K for the graphene on the PI substrate. The transport data is shown over a larger range of temperatures in the SI Section, Figure S4.

The behavior of LPE graphene trending towards lower resistances at higher temperatures has also been observed by others[59]. Regardless, the samples were still conducting at extremely low temperatures, where $R_{Dynamic}$ was ~ 53.4 kΩ at 4 K on $SiO_2$/Si substrates, which decreased to ~ 20 kΩ at 300 K. The higher porosity of solution-exfoliated graphene may yield a greater flake-to-flake separation at lower temperatures due to thermally-induced mechanical contraction. This increases the energy barrier for carriers for intra-flake transport, and thus the $R_{Dynamic}$ increases at low temperatures. This is a characteristic feature of conductors whose transport is governed by a defect-mediated hopping mechanism. Nevertheless, additional measurements should be done on multiple samples under the same conditions to allow comparison between substrates with significance.

**2.2 Inkjet-printed conductors for strain-based biosensing**

A primary advantage of inkjet printing is the ease with which rapid prototyping is possible, allowing a variety of patterns over a broad spectrum of substrates[39,43]. The Ag/Ti electrodes (100 nm/10 nm) used in our strain-sensing experiments as the contact electrodes, were deposited on flexible PI film through a shadow mask, as shown in **Figure 3(c).** The insets of **Figure 3(c)** show the process flow for the fabrication of our strain sensor, for which the bare PI substrate (bottom) and respective shadow mask (top) is shown prior to PVD deposition of the electrodes in **(i)**, after the deposition of the Ag/Ti contact electrodes in **(ii),** where the flexibility of the patterned contact pads is clearly visible; finally in **(iii),** an individual constituent electrode pair cut out to ~ 15 mm squares ready for inkjet deposition is seen. Each pair of electrode pads had a spacing of ~ 4 mm.

A conductive line of graphene was then dispensed across one pair of electrodes in a 7x2 $mm^2$ path via inkjet printing to act as a graphene resistive network. The Cyrene ink used for printing was comprised of ~ 0.1 mg/mL CAB (CAS: 9004-36-8, Thermo Scientific, Catalog No. 404255000) and 25 mg/mL graphite powder ground from graphite rods (CAS: 7782-42-5, Sigma-Aldrich, Product No. 496553) suspended in ≥ 98.5% purity Cyrene (CAS: 53716-82-8, Sigma-Aldrich, Product No. 807796). The graphene lines were printed using a total of five printing passes with the printer settings noted in the Methods Section, where the cartridge and platen were both heated during printing.

Static and dynamic bending measurements were conducted using a Keithley 2400 source meter interfaced with LabView for data acquisition to record the current sweep over time, for a given bias voltage *V*. The printed graphene resistive network was bent in various directions, as shown in **Figure 3(d).** A change in resistance was observed upon bending the device in the concave direction (printed lines in compression), as shown in **Figure 3(d)-(i)**, which resulted in a lower resistance than the device at rest, **Figure 3(d)-(ii)**, and a convex configuration, shown in **Figure 3(d)-(iii) (**printed lines in tension), where a higher resistance was seen compared to the device in the relaxed state. The compressed case likely results in reduced membrane-to-membrane separation between the graphene flakes, thereby reducing the resistance, or equivalently increasing conductivity[3]. The corresponding time-dependent current response for the three cases, concave, relaxed, and convex, are seen in **Figure 3(e)**, where the data show the higher current levels for the concave case (film in compression) compared to the convex case (film in tension). The interface between the Ag/Ti and the printed lines after bending can be observed in **Figure 3(f)**, where no visible damage is observed to the printed graphene film as a result of the instrumentation contacts placed there during the electrical characterization of the devices, validated through the low and high-

magnification optical microscopy images in **(i)** and **(ii)**. Next, the device was left attached to the measurement system and allowed to sit in ambient conditions and measurements were taken at equal intervals, analogous to the 24 hour electrode test conducted in **Figure S1(d)** in the SI Section.

The long-term stability of these devices is first suggested by the data in **Figure 3(g)**, which indicates they are relatively uniform under similar conditions, as opposed to the gel electrodes' slightly bimodal response over time, detailed in the SI section. Effects seen during the dynamic bending tests are corroborated with the static I-V response captured in **Figure 3(h)** corresponding to the bending configurations shown in **Figure 3(d)**. Though the response agrees with the dynamic results of **Figure 3(e)**, it is interesting to note that the current during the relaxed state appeared to depend on its previous state, as the current immediately after the concave state was higher than that after the convex state; this may imply there is a mild memory effect, possibly arising from the slightly porous nature of the films, where the spacing between the randomly oriented membranes may not be exactly the same as the initial state. Since these devices were manually bent, there may be small variations in user technique such as dissimilar bending angles, minor twisting of the device, or variations in the amount of time the device spent in each position throughout the 24 hours that could artificially create differences in the $R_{Dynamic}$ but for the purposes of this preliminary demonstration study, the data suggest these electrodes to show a fairly stable response with time.

After the strain sensing response was verified for our Cyrene-graphene ink-jet printed film, a 50 mm long conducting line was printed on a 60 mm strip of PI film without metal conducting pads for ease of wearability of the electrodes. Here we validate flexion motion detection of the proximal interphalangeal joint, using additively manufactured inkjet-printed Cyrene-based

graphene strain sensors on flexible substrates, a first such study. This extended PI strain sensor was formed using the same printer settings as the 15x15 $mm^2$ electrode pads, and the printed lines here were 2 mm in width. Current measurements were taken along the length of the extended substrate at varying probe distances from 5 mm up to 50 mm, where once again the $R_{dynamic}$, was calculated for each of the spatially spaced points used for the probing measurements, as shown by the data in **Figure 4(a)**. Unsurprisingly, the $R_{dynamic}$ demonstrated a largely linear response in accordance with Ohm's Law. This substrate could also be bent in similar configurations to the sensor pertaining to **Figure 4**. Specifically, **Figures 4(b)-(i), (ii),** and **(iii)** correspond one-to-one, with the data obtained in **Figures 3(d)-(i), (ii),** and **(iii),** for concave (film in compression), relaxed, and convex (film in tension), respectively.

This elongated resistive network allowed the strain sensor to be worn on the finger, where flexible 30-gauge wires were attached to either end of the printed graphene with double-sided carbon tape and then further adhered using insulating electrical tape. It was then fastened to the finger with pliant Teflon tape. Measurements of the finger in its straight position (**Figure 4(c)**) or bent (**Figure 4(d)**), correspond equivalently to the strain sensor in its relaxed and convex (film in tension) configurations, respectively. The device further validated previous findings during the static bending tests conducted from 0 V to 10 V, which yielded a decrease in current when the finger was bent, as shown in **Figure 4(e).**

These effects were more pronounced through our manual time-dependent dynamic tests, represented by the data in **Figure 4(f)**, where the current drops during bending. Incidentally, these dynamic tests resulted in a more pronounced drop in current than was evident through the static bending tests in **Figure 4(e)**.

In order to develop a more robust system to gauge the sensor's ruggedness and repeatability, a Cycling Automator was designed, pictured schematically in **Figure 4(g)**. This instrumentation utilizes an Arduino UNO microcontroller with a VL6180 Time-of-Flight sensor for measurement of the bending angle, and a servo motor to actuate the bending mechanism, where the circuit board connections are shown on the right. This system enabled repeated bending cycles of the strain sensor to be conducted over the course of minutes to hours, keeping the bending conditions identical, while utilizing a 30-gauge flexible wire and light-weight carbon-tape to form an intimate contact, and to overcome the limitations posed by the use of rigid and heavy alligator clips which may interfere with the sample's intrinsic strain-induced sensing mechanism. One cycle of the actuation is defined by a period that starts when the assembly begins to move together, includes a momentary pause, and then moves back to rest, with the strain sensor restored to a neutral position. These cycles may be repeated as many times as desired, and as such, 100 convex and concave bending cycles were performed on a truncated strain sensor at a maximum 90° bending angle, demonstrated by the envelope of cyclical switching data in **Figure 4(h)**.

It is interesting to note that while the sensor returned to the same level during the resting portion of the cycles, the magnitude of these levels depends on which configuration the sensor was being bent in. As can be seen more clearly in the inset of **Figure 4(h)**, when the sensor was in the concave position, corresponding to compression, the current would increase relative to the sensor's relaxed position. However, in the convex position, corresponding to tension of the graphene resistive network, the current would decrease relative to relaxation. To ensure that the results of these tests were a product of the graphene resistive network, the mechanism was also tested with a reference strip of the bare PI substrate, without any film deposited. Although there was a small amount of current present during movement for the bare PI substrate (**Figure 4(i)**), the peak-to-

peak amplitude of this current was negligible (few hundred nanoamps), and there was no noticeable pattern when there was no connection at all. While these results further corroborate our previous findings through manual testing, we also demonstrate the robustness of our sensors through repeated bending cycles performed with our Automator, which should position these devices well for further translational applications towards sensor arrays and networks for human-machine interfaces.

Although the Cycling Automator marks an improvement over manual bending, additional measures can be adopted in future tests to make the contacts more robust for even longer duration testing. Due to their heavy weight and rigidity, alligator clips present problems either by slipping or by creating localized areas of compression and tension when the device is bent in the opposite configuration. Additionally, the large effective area and hardness of the clips may lead to damage at the contacts for longer duration testing, though we did not observe this over the 100 cycles tested in our current experiments. Alternative contact strategies may include the use printed circuit board (PCB) spring contacts—although many are not designed for substrates as thin as PI and may need spacers to allow a connection. Other alternatives may include the adaptation of a flexible printed circuit connector that would traditionally also be PCB-mounted.

## 3. Summary and Conclusions

Successful inkjet-printing of Cyrene-based graphene ink was demonstrated in this work, using five or fewer passes towards highly flexible graphene-based strain sensors and their potential for integration into prosthetic control and multi-axial biosensing in future studies. This printed ink is not only sustainably produced, but unlike traditional solvents for liquid-phase exfoliated graphene, it is also non-toxic. Moreover, Cyrene is capable of higher flake density than other solvents[19],

allowing for fewer printing passes to realize conductive films. While conductivity was mostly temperature independent down to 100 K, below 100 K, the conductivity was found to decrease; this may be explained on the basis of increased membrane-to-membrane separation due to contraction at low-temperatures. Because of its non-toxicity, Cyrene holds great promise towards the production of low-cost wearable electronic devices when compared to more expensive manufacturing methods such as CVD or low-scale methods such as mechanical exfoliation. The environmentally friendly and non-toxic nature of this solvent has promise not only for wearables, but also in agricultural and food industries where sensors need to be safe for potential contacts made to food supplies. This study is among the first to demonstrate inkjet-printed Cyrene-based graphene ink, one of few to demonstrate all-graphene strain sensing[4], and one of many in succession towards the progress of LPE biosensing devices.

## 4. Methods

### Device fabrication

The Cyrene ink was horn tip sonicated for 17 hours and centrifuged at 2000 rpm for 10 minutes, where the removed supernatant was filtered through a 0.45 μm filter for printing. A Dimatix Materials Printer DMP-2850 with 1.5 ml ink cartridges and compatible printheads purchased from the manufacturer was used for inkjet printing. Printing typically used 30 V amplitude, 28 kHz drop frequency, and 15 μm drop spacing. The jetting waveform featured three steps with a slew rate of 2.00 between each one; the first level lasted 3.39 μs at 0% of the set voltage, which then increased to the first step at 100% of the set voltage for 4.67 μs. The second step lasted 2.94 μs at 67% of the set voltage before transitioning to the third step at 20% of the voltage for 0.51 μs, resetting to the baseline to prime the cartridge for the next drop. The platen was heated to 60°C and the cartridge to 40°C to reduce ink viscosity and facilitate the solvent drying process after printing.

An initial 30 μm conditioning layer was used to promote adhesion of the Cyrene ink to account for the high γ of the ink and high surface energy of the PI substrate. After printing, the inks were thermally annealed at 200°C for two hours, and then photonically cured with a NovaCentrix PulseForge Invent system at 450 V for 2000 μs per flash with 15 μpulses, and a 50% duty cycle for a total of 10 repetitions at 1.02 J/cm$^2$ per flash.

## Data availability

The data that support the findings of this study are available upon the request from the corresponding Author.

## Acknowledgements

We are extremely grateful to the Office of Naval Research (ONR) grant number ONR N00014-19-1-2142 and the US Department of Energy (DOE) grant number DE-NA0004114 who provided funding support that enabled us to pursue this work. We would also like to extend special thanks to Silvino Bastos, Utsab Kafley and Carlos Padilla from the University of North Texas for their input in some of the experimental set-ups and lab assistance. Finally, we would like to express our gratitude to Dr. Xiao Li and Tejal Pawale of the University of North Texas for their assistance in measuring the contact angle of the inks.

## Author Contributions

A.B.K. conceived the experiments, provided supervisory support for the experiments and results analysis, and reviewed and edited the manuscript. A.R.T. conducted majority of the experiments, optimized inkjet printing parameters for Cyrene, analyzed results, and drafted the manuscript. M.H. designed and implemented the cyclical testing apparatus. S.A. and J.M. contributed to

Raman spectroscopy results and development of ink recipes. B.J. performed photonic curing of the samples and assisted in some of the figure edits.

## Competing interests

The authors declare that they have no competing financial interests.

## REFERENCES


1. H. Yang and W. Wu, *Frontiers in Electronic Materials,* 2022, **2,** 1-8.
2. M. R. Haque, G. Berkeley and X. Shen, *Sensors,* 2023, **23,** 938.
3. H. Chen, F. Zhuo, J. Zhou, Y. Liu, J. Zhang, S. Dong, X. Liu, A. Elmarakbi, H. Duan and Y. Fu, *Chemical Engineering Journal (Lausanne, Switzerland : 1996),* 2023, **464,** 142576.
4. Sungwoo Chun, Yeonhoi Choi and Wanjun Park, *Carbon,* 2017, **116,** 753–759.
5. I. Y. Kuo and B. E. Ehrlich, *Cold Spring Harbor Perspectives in Biology,* 2015, **7,** a006023.
6. M. B. I. Raez, M. S. Hussain and F. Mohd-Yasin, *Biological Procedures Online,* 2006, **8,** 11–35.
7. R. Merletti, M. Aventaggiato, A. Botter, A. Holobar, H. Marateb, and T. M. Vieira, *Crit. Rev. Biomed.* Eng. 2010, **38**, 305-45.
8. F. J. Romero, E. Castillo, A. Rivadeneyra, A. Toral-Lopez, M. Becherer, F. G. Ruiz, N. Rodriguez and D. P. Morales, *Npj Flex Electron,* 2019, **3,** 1–6.
9. M. Boyer, L. Bouyer, J. Roy and A. Campeau-Lecours, *Sensors,* 2023, **23,** 2927.
10. D. Esposito, J. Centracchio, P. Bifulco and E. Andreozzi, *Sci Rep,* 2023, **13,** 7768.
11. L. Ko, C. Su, P. Liao, J. Liang, Y. Tseng and S. Chen, *JNE,* 2021, **18,** 46060.
12. T. Cui, D. Li, X. Huang, A. Yan, Y. Dong, J. Xu, Y. Guo, Y. Wang, Z. Chen, W. Shao, Z. Tang, H. Tian, Y. Yang and T. Ren, Applied Sciences, 2022, 12, 4526.
13. X. Huang, L. Liu, Y. H. Lin, R. Feng, Y. Shen, Y. Chang and H. Zhao, Science Advances, 2023, 9, eadh9799.
14. F. Torrisi, T. Hasan, W. Wu, Z. Sun, A. Lombardo, T. S. Kulmala, G. W. Hsieh, S. Jung, F. Bonaccorso, P. J. Paul, D. Chu and A. C. Ferrari, *ACS Nano,* 2012, **6,** 2992–3006.
15. X. Huang, T. Leng, M. Zhu, X. Zhang, J. Chen, K. Chang, M. Aqeeli, A. K. Geim, K. S. Novoselov and Z. Hu, *Sci Rep,* 2015, **5,** 18298–18298.
16. S. Tkachev, M. Monteiro, J. Santos, E. Placidi, M. B. Hassine, P. Marques, P. Ferreira, P. Alpuim and A. Capasso, *Advanced Functional Materials,* 2021, **31,** 3287.
17. D. Kuzum, H. Takano, E. Shim, J. C. Reed, H. Juul, A. G. Richardson, J. de Vries, H. Bink, M. A. Dichter, T. H. Lucas, D. A. Coulter, E. Cubukcu and B. Litt, *Nature Communications,* 2014, **5,** 5259–5259.
18. N. Celik, N. Manivannan, A. Strudwick and W. Balachandran, *Nanomaterials,* 2016, **6,** 156–156.
19. K. Pan, Y. Fan, T. Leng, J. Li, Z. Xin, J. Zhang, L. Hao, J. Gallop, K. S. Novoselov and Z. Hu, *Nat Commun,* 2018, **9,** 5197–10.
20. P. He, J. Cao, H. Ding, C. Liu, J. Neilson, Z. Li, I. A. Kinloch and B. Derby, *ACS Applied Materials & Interfaces,* 2019, **11,** 32225–32234.
21. Y. Xu, H. Cao, Y. Xue, B. Li and W. Cai, *Nanomaterials,* 2018, **8,** 942.
22. A. Citarella, A. Amenta, D. Passarella and N. Micale, *International Journal of Molecular Sciences,* 2022, **23,** 15960.
23. M. Michel, C. Biswas and A. B. Kaul, *Applied Materials Today,* 2017, **6,** 16–21.
24. Y. Z. N. Htwe, M. K. Abdullah and M. Mariatti, *Synthetic Metals,* 2021, **274,** 116719.
25. R. F. Hossain, M. Min, L. Ma, S. R. Sakri and A. B. Kaul, *Npj 2D Mater Appl,* 2021, **5,** 1–12.
26. M. Min, R. F. Hossain, N. Adhikari and A. B. Kaul, *ACS Applied Materials & Interfaces,* 2020, **12,** 10809–10819.
27. F. Mouhat, F. X. Coudert and M. L. Bocquet, Nature Communications, 2020, 11, 1566.

28. A. Rossi, E. Alladio, D. Drobne, V. Hodoroaba, K. Jurkschat, V. Kononenko, L. A. Madbouly, P. Mrkwitschka, S. Novak, J. Radnik, Š Saje, R. Santalucia, F. Sordello and F. Pellegrino, Sci Rep, 2024, 14, 22381.
29. P. Phukan, R. Narzary and P. P. Sahu, Materials Science in Semiconductor Processing, 2019, 104, 104670.
30. S. Pei and H. M. Cheng, Carbon, 2012, 50, 3210–3228.
31. A. S. Joshi, E. Elamurugu and Leela.S, Chemical Physics Impact, 2024, 9, 100667.
32. C. Grune, J. Thamm, O. Werz and D. Fischer, *Journal of Pharmaceutical Sciences,* 2021, **110,** 959–964.
33. J. Fernandes, S. S. Nemala, G. De Bellis and A. Capasso, Frontiers in Chemistry, 2022, 10, 878799.
34. G. Rivers, J. S. Austin, Y. He, A. Thompson, N. Gilani, N. Roberts, P. Zhao, C. J. Tuck, R. J. M. Hague, R. D. Wildman and L. Turyanska, *Additive Manufacturing,* 2023, **66,** 103452.
35. W. Zeng, L. Shu, Q. Li, S. Chen, F. Wang and X. Tao, *Advanced Materials,* 2014, **26,** 5310–5336.
36. Y. Bai, T. Xu and X. Zhang, *Micromachines,* 2020, **11,** 60.
37. R. F. Hossain, I. G. Deaguero, T. Boland and A. B. Kaul, *Npj 2D Mater Appl,* 2017, **1,** 28.
38. B. Ali, H. Cheraghi Bidsorkhi, A. G. D'Aloia, M. Laracca and M. S. Sarto, *Sensors and Actuators Reports,* 2023, **5,** 100161.
39. D. Wattanaprakornkul, I. Cathers, M. Halaki and K. A. Ginn, Journal of Science and Medicine in Sport, 2011, 14, 376–382.
40. J. W. L. Pau, S. S. Q. Xie and A. J. Pullan, TBME, 2012, 59, 2586–2593.
41. I. Poitras, M. Bielmann, A. Campeau-Lecours, C. Mercier, L. J. Bouyer and J. Roy, Sensors, 2019, 19, 1885.
42. Y. Blache, F. Dal Maso, L. Desmoulins, A. Plamondon and M. Begon, Journal of Electromyography and Kinesiology, 2015, 25, 355–362.
43. J. Wu, M. Lin, X. Cong, H. Liu and P. Tan, *Chemical Society Reviews,* 2018, **47,** 1822–1873.
44. A.C. Ferrari, J.C. Meyer, V. Scardaci, C. Casiraghi, M. Lazzeri, F. Mauri, S. Piscanec, D. Jiang, K.S. Novoselov, S. Roth, and A.K. Geim, *Phys. Rev. Lett.* 2006, **97**, 187401.
45. J. N. Coleman, Y. Hernandez, V. Nicolosi, M. Lotya, F. M. Blighe, Z. Sun, S. De, I. T. McGovern, B. Holland, M. Byrne, Y. K. Gun'Ko, J. J. Boland, P. Niraj, G. Duesberg, S. Krishnamurthy, R. Goodhue, J. Hutchison, V. Scardaci and A. C. Ferrari, *Nature Nanotech,* 2008, **3,** 563–568.
46. A. C. Ferrari and D. M. Basko, *Nature Nanotech,* 2013, **8,** 235–246.
47. David Tuschel, Spectroscopy, 2016, 31, 14–23.
48. D. Marlina, M. Novita, M. T. Anwar, H. Kusumo and H. Sato, Journal of Physics. Conference Series, 2021, 1869, 12006.
49. S. Wang, L. Wan, D. Li, X. Chen, X. Xu, Z. C. Feng and I. T. Ferguson, *Frontiers in Materials,* 2022, **9,** 924143.
50. I. Calizo, A. A. Balandin, W. Bao, F. Miao and C. N. Lau, *Nano Letters,* 2007, **7,** 2645–2649.
51. K. Jayanand, S. Chugh, N. Adhikari, M. Min, L. Echegoyen and A. B. Kaul, *Journal of Materials Chemistry. C,* 2020, **8,** 3970–3981.
52. M. Michel, C. Biswas, C. S. Tiwary, G. A. Saenz, R. F. Hossain, P. Ajayan and A. B. Kaul, *TDM,* 2017, **4,** 25076.
53. D. Barmpakos, V. Belessi, R. Schelwald and G. Kaltsas, *Nanomaterials,* 2021, **11,** 2025.
54. M. Michel, J. A. Desai, C. Biswas and A. B. Kaul, *NANO,* 2016, **27,** 485602.

55. S. Krainer, C. Smit and U. Hirn, *RSC Advances,* 2019, **9,** 3178–31719.
56. A. Bastola, Y. He, J. Im, G. Rivers, F. Wang, R. Worsley, J. S. Austin, O. Nelson-Dummett, R. D. Wildman, R. Hague, C. J. Tuck and L. Turyanska, *Materials Today Electronics,* 2023, **6,** 100058.
57. D. Lohse, *Annual Review of Fluid Mechanics,* 2022, **54,** 349–382.
58. H. Wang and P. R. Brito-Parada, *J. Colloid Interface Sci.,* 2021, **587,** 14–23.
59. D. Kong, L. T. Le, Y. Li, J. L. Zunino and W. Lee, *Langmuir,* 2012, **28,** 13467–13472.

## LIST of FIGURES

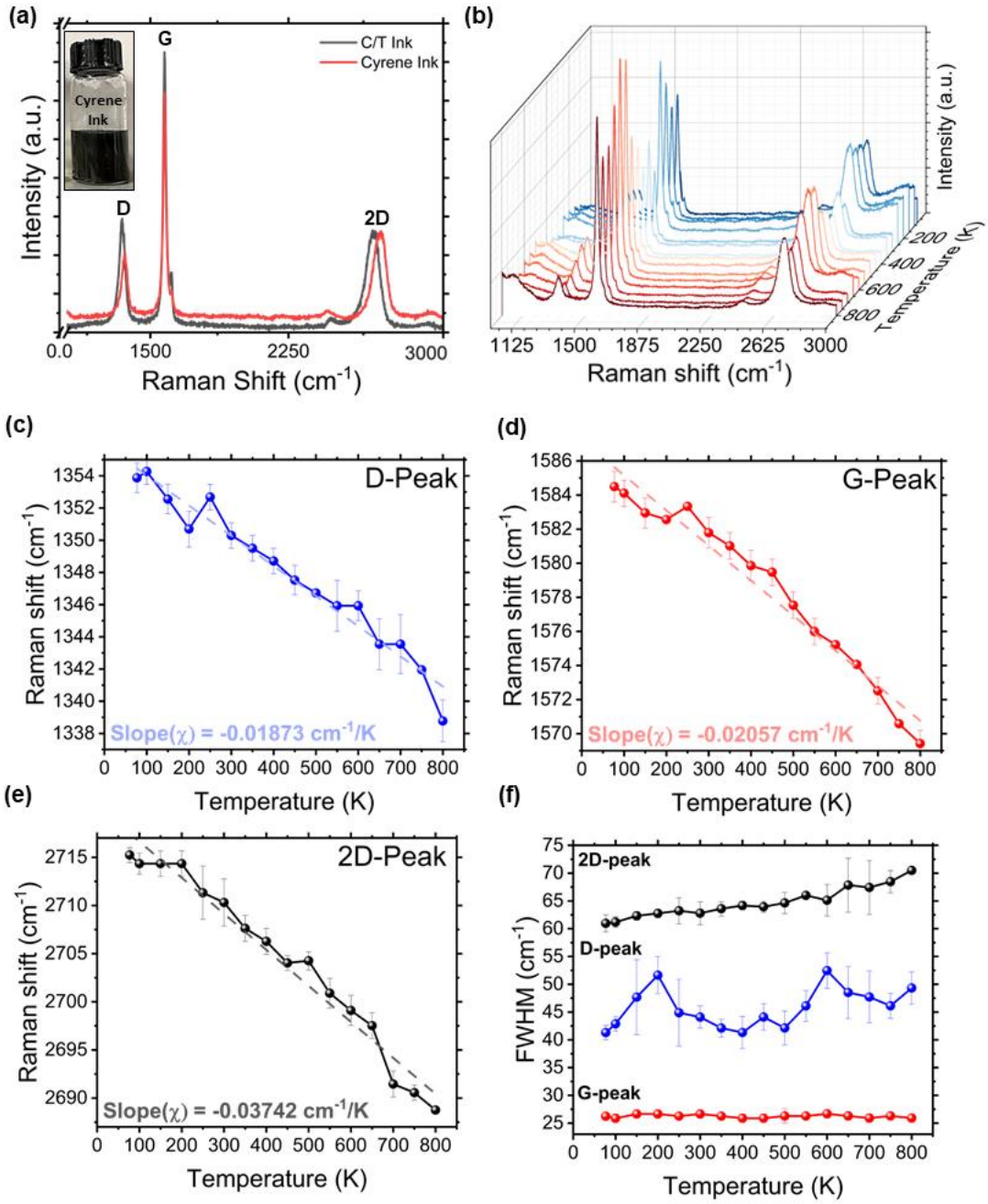


**Figure 1. (a)** Raman spectroscopy comparison of C/T-based and Cyrene-based graphene inks on $SiO_2$/Si substrates, demonstrating some differences in the graphitic peak locations for the two solvents. **(b)** Temperature-dependent Raman spectroscopy of Cyrene-based graphene film from 77 K to 800 K in atmospheric air. **(c)-(e)** Averaged Raman shifts between 4 locations on the sample attributed to the peak positions of the D-peak, G-peak, and the 2D-peaks, respectively, showing red-shifting of all the peaks as temperature increased. Error bars represent *1-σ* variations about the mean. **(f)** The FWHM of the Raman peaks was temperature-invariant with an exception for the

2D-peak which experienced slight peak broadening with increasing temperature, likely due to phonon-mediated interactions. Our data suggest the Cyrene-based printed graphene films are robust to serve as active elements in extreme thermal environments, potentially considered for sensors.

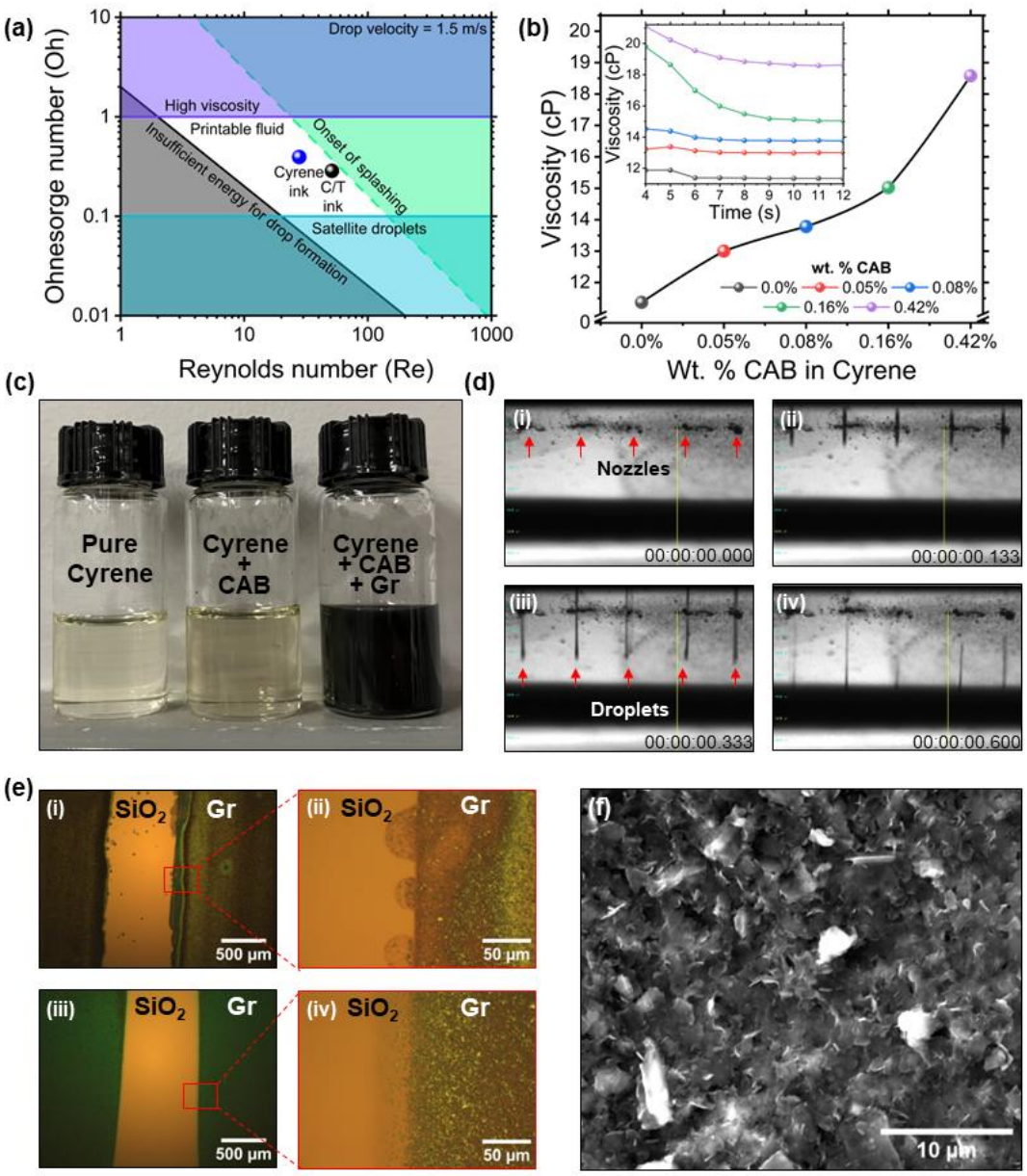


**Figure 2. (a)** Plot of *Oh* vs *Re* with Cyrene and C/T inks plotted within the printable region. **(b)** Viscosity $\eta$ variation with increasing additions of CAB in Cyrene after stabilization. Inset shows $\eta$ of Cyrene with increasing CAB concentrations over time with the Rheometer. **(c)** Physical variations in ink appearance with pure Cyrene which is transparent (left-vial), addition of the CAB at 0.08 wt.% to the Cyrene, where a slight color change is evident (middle-vial); the right-most vial shows a significant change from translucent to opaque black with the addition of graphite/graphene. **(d)** Jetting progression of Cyrene ink over a period of 600 ms. **(e)** Printed line-edge resolution of the C/T ink at: **(i)** low and **(ii)** high-magnifications, and similarly for Cyrene ink at: **(iii)** low and **(iv)** high-magnifications, respectively. Labelled are the underlying substrate with $SiO_2$ and the printed graphene (Gr) film regions. Minimal stray droplets are evident with the Cyrene-graphene ink in **(iii)** and **(iv)**, with a cleaner line-edge resolution and pattern fidelity,

compared to the C/T ink which exhibits a compromised line-edge resolution. **(f)** SEM image of inkjet-printed Cyrene-graphene ink reveals the printed film's morphology to be dense.

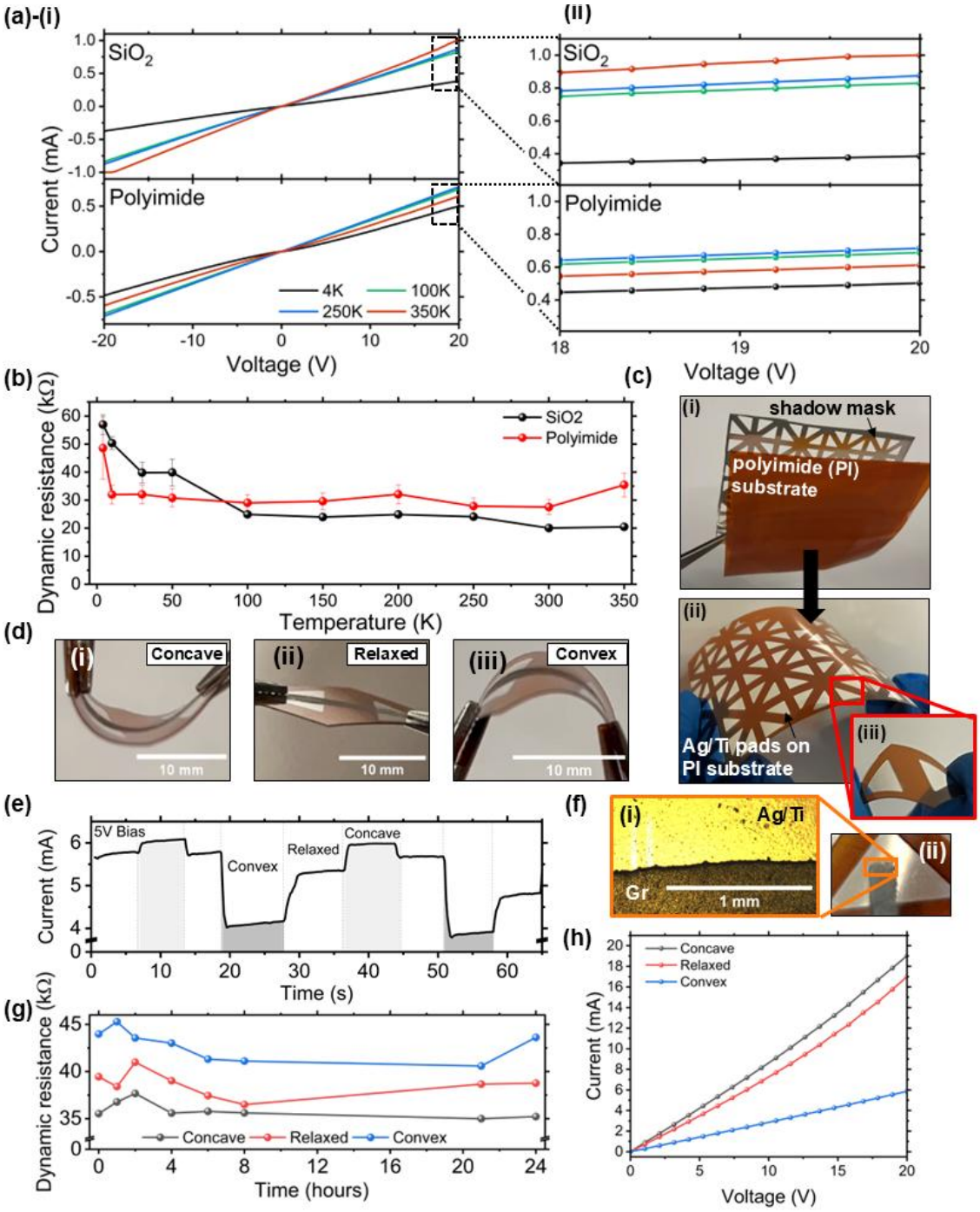


**Figure 3. (a)-(i)** The typical I-V characteristic of inkjet-printed Cyrene-graphene film measured in vacuum at four different temperatures on an $SiO_2$/Si substrate (top) and on a PI film (bottom) as the substrate; magnified view is seen in **(ii)** from 18 V to 20 V. The current was higher for the graphene film printed on the $SiO_2$/Si substrate compared to the film printed on a PI substrate. **(b)** Calculated $R_{dynamic}$ of graphene on $SiO_2$/Si and PI substrates as a function of temperature, where the $R_{dynamic}$ decreased as temperature increased up to ~ 10 K for the PI substrate, and up to ~ 100 K for the $SiO_2$/Si substrate. Beyond these temperatures, the $R_{dynamic}$ was largely temperature

invariant. Error bars represent the 1-sigma (1-σ) standard deviation of the resistance calculated across the entire voltage sweep in **(a)**. **(c)** Process flow of the PVD deposited Ag electrodes on a PI substrate which serve as the contacts to the flexible strain-sensing devices: **(i)** bare PI film placed adjacent to the shadow mask; **(ii)** deposited Ag/Ti pads on PI; **(iii)** magnified view of a single Ag/Ti electrode pair used for printing and the strain-sensing experiments. **(d)** Printed graphene on Ag/Ti electrodes in **(i)** concave, **(ii)** relaxed, and **(iii)** convex configurations, respectively. **(e)** Temporal response of the current change in printed device, where increased current was observed during the concave configuration, while decreased current was observed in the convex configuration, at a bias of ~ 5 V. **(f)** Overlap region viewed under an optical microscope between the Ag/Ti electrodes and the overlying printed graphene film at **(i)** high-magnification, and **(ii)** low-magnification, which shows the graphene film is largely unperturbed as a result of the instrumentation contacts placed there during electrical characterization of the devices. **(g)** Calculated $R_{dynamic}$ of the printed device with one measurement taken in all three configurations at varying time intervals, which revealed the $R_{dynamic}$ to be largely in-variant with time up to the 24 hours tested, unlike the somewhat time-dependent response measured equivalently for the wet-electrode devices tested in **Figure S1(e)**. **(h)** Single voltage sweep of the printed device during the static bending configurations displayed in (d).

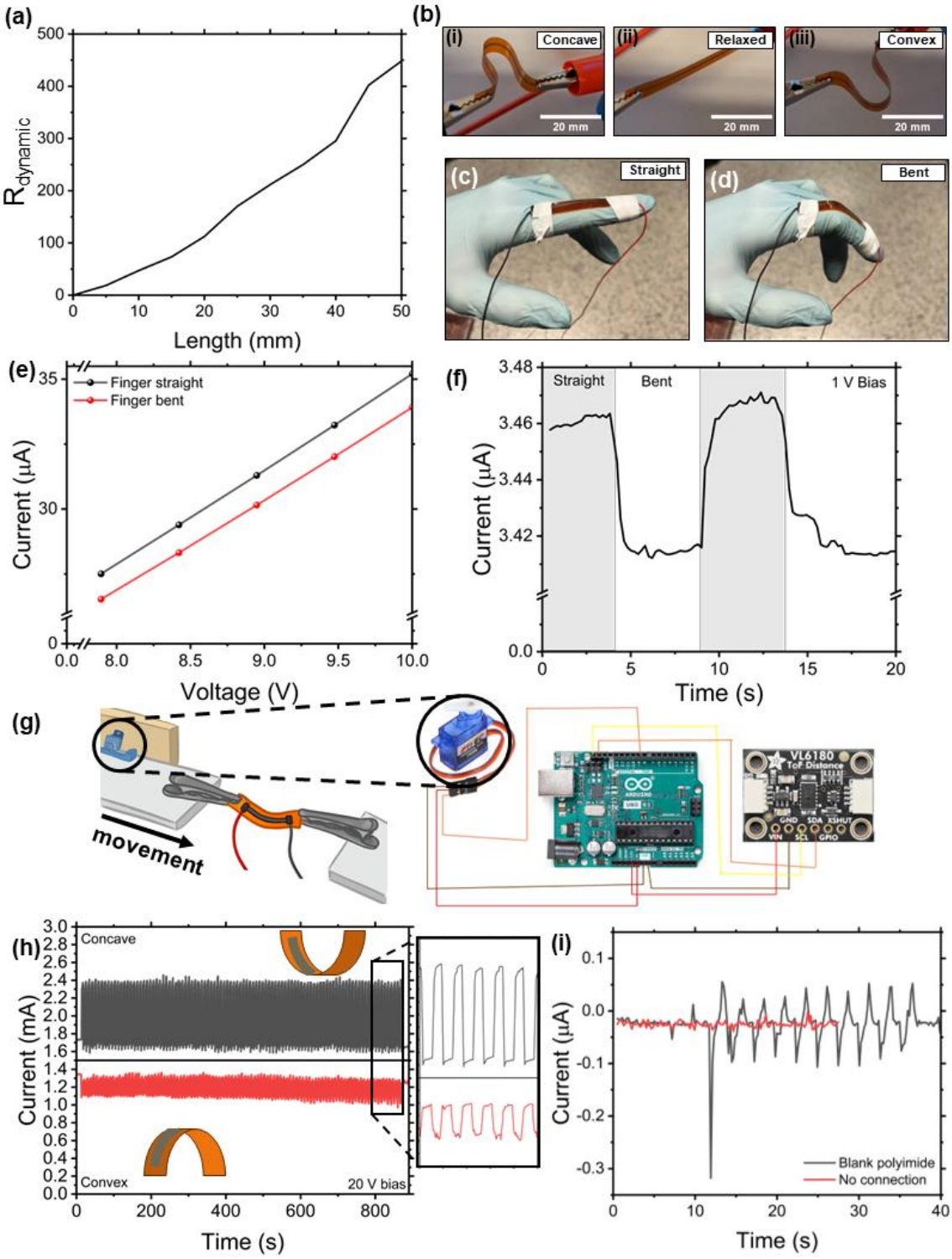


**Figure 4. (a)** Resistance scaling with length of the printed Cyrene-graphene film on the PI substrate, confirming its largely linear response in accordance with Ohm's Law. **(b)** Printed graphene templates on an extended substrate configuration without metal electrodes in **(i)** concave, **(ii)** relaxed, and **(iii)** convex states, respectively. The experimental set-up in **(c)-(d)** was used for flexion motion detection of the proximal interphalangeal joint, with our additively manufactured

inkjet-printed Cyrene-based graphene ink on flexible substrates, where 30-gauge wires were secured to the finger using Teflon and electrical tape. **(e)** Current changes on the extended PI substrate when attached to the finger, demonstrating slightly decreased current in the bent state through this static test. **(f)** Time-dependent dynamic tests, where a pronounced drop in current was seen during bending, with the device held at 1 V bias. **(g)** Configuration and experimental set-up of the in-house Cycling Automator on the left, which used an Arduino and servo motor connected on a circuit board (right). **(h)** Data for 100 cycles is shown through the two envelopes of current polarity (left), with the right inset depicting 5 cycles on an expanded scale for the concave (top) and the convex (bottom) configurations, respectively. **(i)** Cycling data for a bare PI film with clips and with no substrate between the clips validates the stray leakage currents to be negligible (in the hundreds of nanoamperes range, peak-to-peak).

## LIST of TABLES

**Table 1.** Peak positions and intensity ratios of C/T (633 nm laser) and Cyrene ink (532 nm laser) as taken from the Raman measurements conducted at room temperature (**Figure 1(a)**). The Cyrene-graphene ink shows a lower D/G ratio and thus fewer defects, compared to the film exfoliated using C/T solvent.

| | Peak positions ($cm^{-1}$) | | | Ratios | |
|---|---|---|---|---|---|
| **Solvent used for Graphene Film** | **D-peak** | **G-peak** | **2D-peak** | **$I_{2D}/I_G$** | **$I_D/I_G$** |
| **C/T** | 1335.1 | 1580.5 | 2674.7 | 0.36 | 0.41 |
| **Cyrene** | 1350.9 | 1581.2 | 2710.0 | 0.42 | 0.34 |